Mathematical Modeling and Analysis of Electromagnetic Direct Drive Air Compressor

Chunlin Guo, Jiayu Lu ,Wenqing Ge, Xiaochen Zhang and Bo Li

***Abstract*—To accurately simulate the motion characteristics of a reed valve and the changes in the flow field within an exhaust chamber, a fluid-structure coupling model of an electromagnetic direct-drive air compressor during the exhaust process was established and simulated. Using Computational Fluid Dynamics (CFD) software, transient numerical simulations of the flow field were conducted to reduce the computational model's time complexity and provide an immediate analysis of the exhaust process. This paper explores the effects of varying valve lift and relative pressure loss under different valve parameters and exhaust pressure levels. The findings reveal that when the valve plate thickness is 0.2mm and the valve section width is 3.5mm, airflow resistance is significantly minimized. When the valve plate is unloaded, the impact of gas flow restriction on overall gas flow is negligible. This study provides a theoretical basis for designing exhaust valves in electromagnetic direct-drive air compressors. The effectiveness of the designed exhaust valve and the system is verified.**

***Index Terms*—Air valve, Mathematical modeling, Computational Fluid Dynamics (CFD), Fluid-structure coupling**

I. Introduction

The electromagnetic direct drive-air compressor features a more compact structure and higher transmission efficiency due to the omission of the crank connecting rod structure. This design does not compromise the advantageous sealing of traditional reciprocating compressors. The air valve, often referred to as the "heart" of the compressor, is an essential component of the piston compressor, as its performance has a direct impact on energy efficiency. Tongue spring valves, commonly used in small and medium-sized piston compressors due to their simple structure and small clearance volume, are employed in solenoid direct-drive air compressors as exhaust valves [1].

ln the previous century, researchers primarily investigated valve discs by solving differential equations for valve disc and gas state in the cylinder [2-3]. With the advancement of computer technology, computational fluid dynamics (CFD) software is now frequently used to simulate gas flow and the stress and deformation state of the valve plate. LINK et al. discovered that the movement of air valves affects the flow loss and vibration noise of reciprocating compressors [4]. KOPPPULA explored the impact of pressure variations on the motion state of the valve disc [5]. Deng Wenjuan demonstrated that the flow area of the valve correlates with the valve disc's size parameter [6]. Han Baokun analyzed the temporal variation characteristics of valve tongue displacement and inlet flow [7]. Bao Huaiqian determined the fluid flow state changes within the cylinder [8]. Ji Jiang conducted a study on the transient change characteristics of valve disc lift [9].

Our team's proprietary air compressor drive motor ensures swift response and precision. we pair this with an air compressor to establish a novel electromagnetic air compressor employing an electromagnetic linear actuator. The decrease in single-cylinder gas emissions did not notably affect the intake valve's operating conditions while the exhaust valve's environmental changes were substantial. Consequently, a minimal alterations strategy was applied to redesign the latter. This air compressor necessitates a fluid-solid coupling model that brings together Computational Fluid Dynamics (CFD) with conventional modeling methods for accelerated and precise model calculations. By numerically simulating and analyzing the exhaust process of our electromagnetic direct-drive air compressor, we investigate the correlations among valve lift, pressure drop, and various valve settings/exhaust pressures, offering theoretical foundations for compressor exhaust valve designs and validating the design viability of such compressors. Refer to Figure 1 for its structural blueprint.

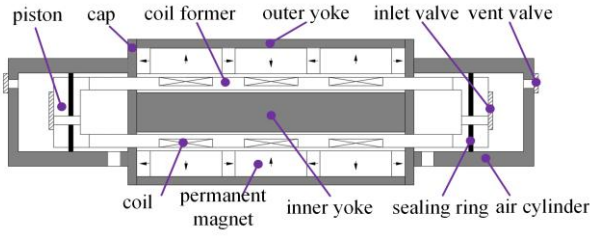

Fig. 1. Schematic diagram of electromagnetic direct drive compressor

II. Fluid-Structure Coupling Model in Exhaust Process

A. An overview of computational fluid dynamics

Computational fluid dynamics can be defined as the numerical simulation of the motion of fluids under the control of fluid motion equations. Therefore, in order to solve fluid motion problems, it is essential to establish the equations that govern fluid motion. As

Manuscript received February 29, 2024; revised January 08, 2025.

This project was supported in part by the National Natural Science Foundation of China (52305265,52375105), the Natural Science Foundation of Shandong Province (ZR2022YQ51), and the Major Science and Technology Innovation Program of Shandong Province (2021CXGC010703).

Guo Chunlin is a PhD candidate at Shandong University of Technology, Zibo 255000 China (e-mail: gcl98love12@163.com).

Jiayu Lu is an associate professor of Vehicle engineering, Shandong Institute of Technology in China, Zibo 255000 China (corresponding author to provide phone: +861599638273; fax: +861599638273; e-mail: lu_j_y@126.com).

Wenqing Ge is a professor of mechanical engineering at Shandong University of Technology, Zibo 255000 China (e-mail: gwq@sdut.edu.cn).

Xiaochen Zhang is a postgraduate student at Shandong University of Technology, Zibo 255000 China (e-mail: 3107244086@qq.com).

Bo Li is a professor of vehicle engineering at Shandong University of Technology, Zibo 255000 China (e-mail: njustlibo@126.com).

fluid mechanics is a branch of mechanics, the motion of fluids is also subject to the laws of physics. The fundamental conservation laws of fluid mechanics include the equations for mass conservation, energy conservation, and momentum conservation.

$$\frac{\partial \rho}{\partial t}+\frac{\partial(\rho u)}{\partial x}+\frac{\partial(\rho v)}{\partial y}+\frac{\partial(\rho w)}{\partial z}=0 \tag{1}$$

equation of continuity：

$$\frac{\partial \rho}{\partial t}+\nabla\bullet(\rho V)=0 \tag{2}$$

Where, ρ represents density; u, v and w represent time as the component of velocity vector in x, y and z directions respectively; t is time.

Energy conservation equation:

$$\frac{\partial(\rho T)}{\partial \mathrm{t}}+\frac{\partial(\rho u T)}{\partial x}+\frac{\partial(\rho v T)}{\partial y}+\frac{\partial(\rho w T)}{\partial z}=$$
$$\frac{\partial}{\partial x}\left(\frac{k}{C_p}\frac{\partial T}{\partial x}\right)+\frac{\partial}{\partial y}\left(\frac{k}{C_p}\frac{\partial T}{\partial y}\right)+\frac{\partial}{\partial z}\left(\frac{k}{C_p}\frac{\partial T}{\partial z}\right)+S_t \tag{3}$$

Where Cp is the specific heat capacity, T is the thermodynamic temperature, and k is the heat transfer coefficient, St which is called the viscous dissipation term

Momentum conservation equation:

$$\begin{cases}\dfrac{\partial(\rho u)}{\partial x}+div(\rho u\boldsymbol{u})=-\dfrac{\partial p}{\partial x}+\dfrac{\partial \tau_{xx}}{\partial x}+\dfrac{\partial \tau_{yx}}{\partial y}+\dfrac{\partial \tau_{zx}}{\partial z}+F\\ \dfrac{\partial(\rho v)}{\partial y}+div(\rho v\boldsymbol{u})=-\dfrac{\partial p}{\partial y}+\dfrac{\partial \tau_{xy}}{\partial x}+\dfrac{\partial \tau_{yy}}{\partial y}+\dfrac{\partial \tau_{zy}}{\partial z}+F_y\\ \dfrac{\partial(\rho w)}{\partial z}+div(\rho w\boldsymbol{u})=-\dfrac{\partial p}{\partial z}+\dfrac{\partial \tau_{xz}}{\partial x}+\dfrac{\partial \tau_{yz}}{\partial y}+\dfrac{\partial \tau_{zz}}{\partial z}+F_z\end{cases} \tag{4}$$

Where, p is the pressure on the fluid element, and τxx, τxy and τyz are the components of the viscous stress τ generated by the molecular viscous action. Fx, Fy, Fz are the force on the micro body, and u is the velocity vector.

B. Establishment of fluid-structure coupling model in exhaust process

The three-dimensional software CATIA is utilized to create the three-dimensional model of the fluid region for the cylinder of an air compressor directly. The three-dimensional model of the cylinder mainly consists of cylinder, inlet and exhaust ports, and the cylinder and valve connection chamber, etc. Catia software is used to establish the cylinder fluid model of the air compressor. The model is imported into Fluent, and the mesh module is used to mesh the fluid model. The piston surface is set as the moving surface, the dynamic layering model is used, and the profile file is used to define the piston movement law. the resulting configuration is shown in Figure 2 below,Once the model is built in the three-dimensional software, it is imported into ANSYS' Fluent unit and then into Geometry.

Given that the fluid domain of the gas movement inside the cylinder is continually changing with the rotation of the crankshaft, dynamic grid technology is implemented during the calculation process. It must be acknowledged that dynamic grid technology necessitates precise grid requirements; otherwise, errors may occur, or the calculation outcomes may not be ideal. Therefore, the quality of the variable volume area of the grid is superior to that of the constant volume area. In recognition of the advantages of using tetrahedral mesh and hexahedral mesh, hexahedral mesh was chosen for in-cylinder fluid simulation in order to produce a structured mesh with regular spacing and a consistent arrangement. By reconstructing the hexahedral mesh, we can simulate the changing process of the fluid domain effectively, improve convergence speed, and shorten calculation time. As for the complex models of the exhaust reed valve and exhaust chamber, they are segmented using tetrahedral mesh due to their intricacy.

Given the fact that the gas changes greatly as it flows through the valve gap, it necessitates a separate region and a smaller grid size. Unstructured grid technology is applied to the complex structure of the valve disc, while structured grid technology is utilized at the gas inlet and outlet where the gas's status changes less, reducing the amount of calculations required. To minimize the data transmission error at the interface, a common node is employed for the grid between different regions.

The boundary of the fluid should be defined after the grid division is completed. The accuracy of defining the boundary is crucial to improve the simulation results' accuracy. Once the cylinder flow field model has been gridded, it is imported into the Set up module. Transient cylinder motion is selected, and the gas is set to be an ideal gas. The fluid movement inside the cylinder falls under unsteady compressible flow. The pressure implicit PISO algorithm is chosen, with the fluid material set to air and gas density set to ideal gas. The standard K-Epsilon turbulence model is applied to the fluid model, while the wall is set as adiabatic without slip. The inlet and outlet boundary of the compressor are defined. The outlet is designated as the pressure outlet, which is 1500KPa.

To accurately simulate the instantaneous changes in the airflow within the air compressor and obtain a motion condition consistent with real-world conditions, it is necessary to incorporate the flow field into a dynamic grid. This approach allows for the fluid and grid models to be adjusted in response to changes in the flow field, ensuring a more accurate simulation. Fluent offers three types of dynamic grid computing: spring-based smoothing, dynamic layering, and local remeshing. These methods provide flexibility in handling different aspects of the flow dynamics. The upward motion of the piston is achieved through the use of the layup model, which is well-suited for this type of movement. Meanwhile, the motion of the valve disc is realized through local redrawing and the elastic approximate smooth model, which allows for precise control over the valve's movement. The move surface type was defined as rigid body motion, with its movement characterized by its profile, ensuring that the simulation accurately reflects the physical behavior of these components.The FSI wall surface's moving mesh was coupled to the system, and the mesh thickness for the two moving grids was set at 0.6mm and 0.3mm, respectively. These settings are chosen to optimize the simulation's accuracy and computational efficiency. Once the grid division is complete, the resulting configuration is shown in Figure 2 below.

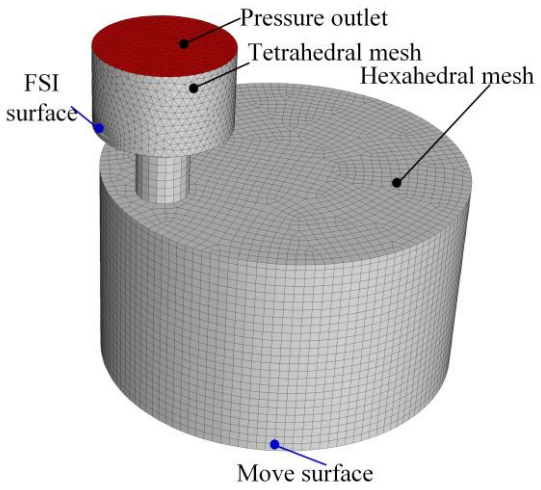

Fig. 2. Schematic diagram of cylinder grid

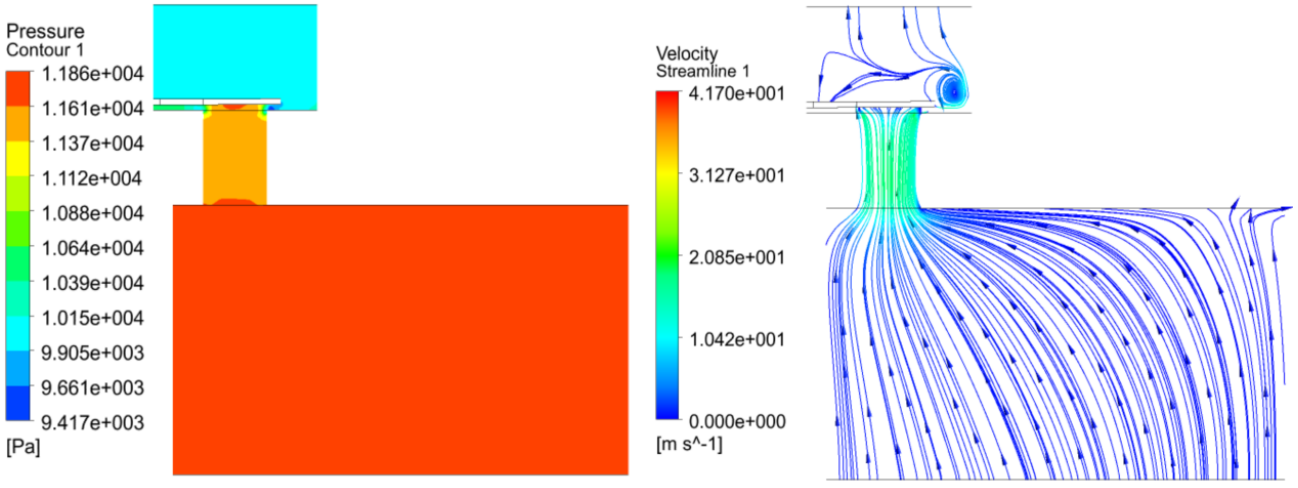

a) t=0.001s

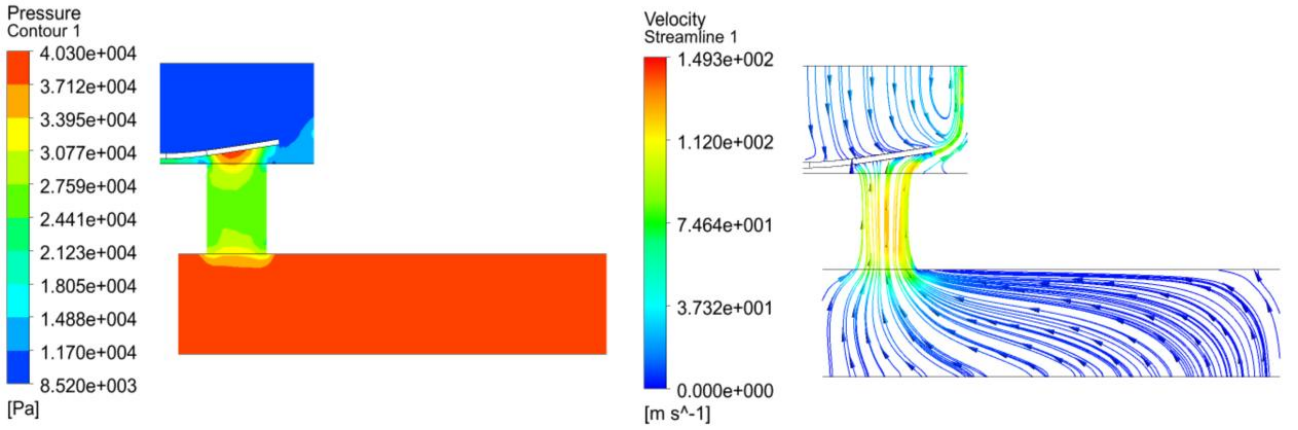

b) t=0.006s

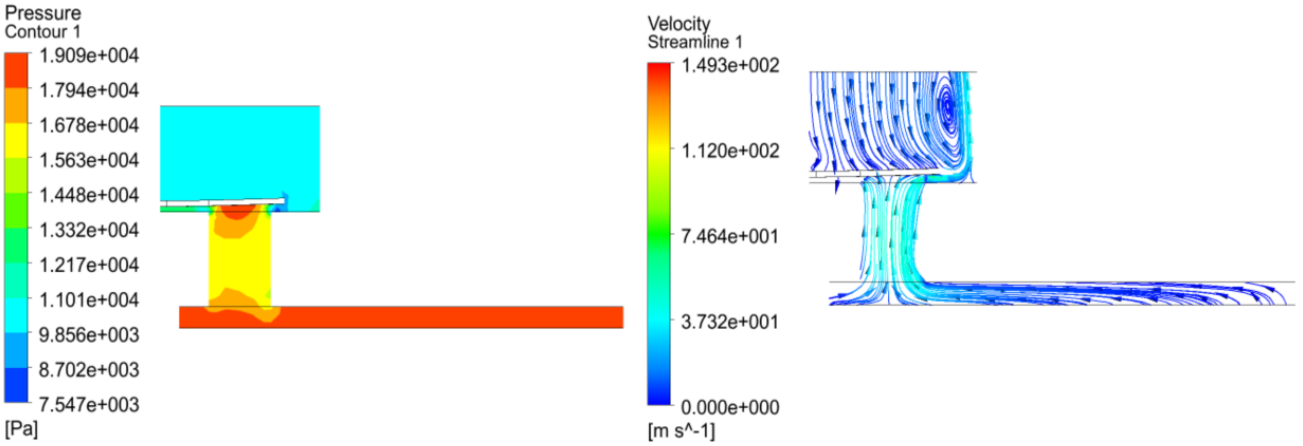

c) t=0.009s

Fig. 3. Pressure nebulae and velocity flow diagrams at different times

III. Exhaust Process Simulation Under Different Parameters

A. *Pressure field and velocity field analysis*

Three moments of t=0.001, t=0.006 and t=0.009 are selected, and the simulated pressure and velocity distribution cloud map is shown in Figure 3 above.

During the exhaust process, a significant pressure exceeding the gas pressure in the exhaust chamber is generated due to the force exerted on the valve disc. By using pressure cloud imagery and flow diagrams, the cause of this elevated pressure can be traced to the impact of gas escaping from the cylinder onto the lower section of the reed valve, which compresses the gas and leads to elevated pressure. The impact pressure of the gas helps maintain the pressure differential between the top and bottom of the reed valve, a crucial aspect of keeping it in an open state. The movement of the valve disc in the exhaust chamber has a profound effect on pressure distribution, resembling the lift curve of the reed valve during fluctuations in flow rate. When gas passes through the spring valve, uneven pressure distribution and significant changes in gas pressure gradients occur within a confined area. As the gas exits the exhaust chamber, the

pressure gradient shifts downward, indicating a decrease in pressure. Consistent with Bernoulli's principle, low pressure prevails within the gas as it emerges from the exhaust chamber. The pressure at the valve port is significantly lower than the cylinder pressure.

As evident from the velocity flow diagram, when the reed valve opening is minimal, the valve outlet exhibits maximum velocity, and there is also a high velocity region at the outlet of the exhaust chamber. Since the valve port area is significantly smaller than the piston's cross-sectional area, it is explicitly clear that the velocity in the valve port is much higher than that in the cylinder throughout the entire exhaust process. The gas generates a vortex above the valve disc, and the closer the flow path in the vortex to the valve disc, the higher the gas flow velocity. It can be inferred that the energy of the vortex primarily derives from the viscous forces of the exiting gas.

B. Simulation of exhaust process under different valve thickness

Reed valve structure significantly impacts max stress and spring stiffness during opening. Spring stiffness crucial to valve performance; deviating from the ideal leads to issues like delayed operation, vibration, and shorter fatigue lifespan. Valve thickness, in accordance with the valve deformation theory, vital. Conventional reed valves come in two thicknesses - 0.2mm and 0.3mm. This research compared the performance of these valves in terms of pressure loss and lift.

The results of the comparison are depicted in Figure 4, which illustrates the relative pressure loss and valve disc lift for each thickness.

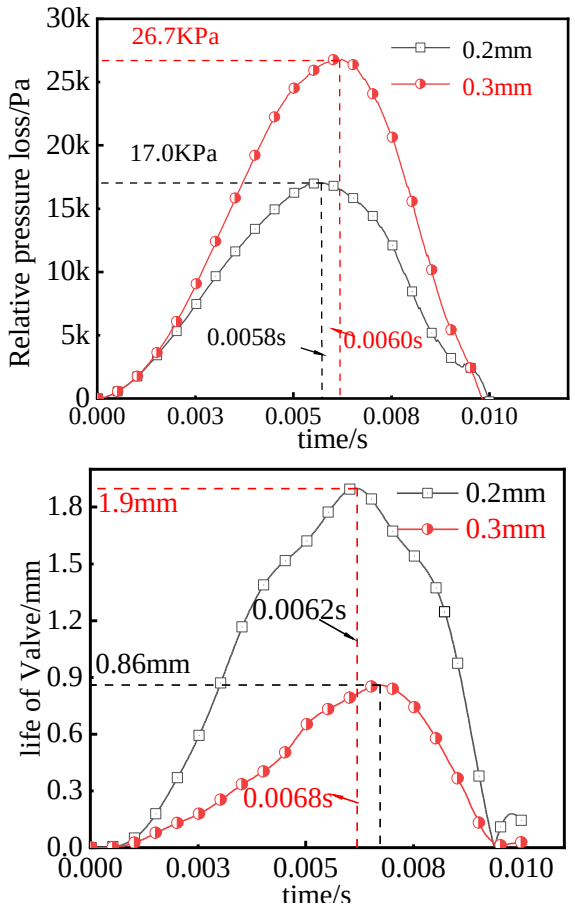

Fig. 4. Valve lift and pressure loss under two thicknesses

TABLE I
MAXIMUM LIFT AND MAXIMUM RELATIVE PRESSURE LOSS OF VALVE

Valve plate thickness (mm)	Valve lift(mm)	Relative pressure loss(MPa)
0.2	0.59	0.04
0.3	1.43	0.17

Simulation demonstrated a pressure drop of 17,000 Pa when using 0.2mm thickness, increasing to 26,700 Pa (33% and 20% of the exhaust pressure), using 0.3mm thickness. Max respective valve lift equaled 1.9mm and 0.86mm, and there were no instances of double opening. As valve thickness augmented, so did the cylinder flow field maximum pressure due to higher spring force. However, high spring force could hinder normal valve operation necessitating extra gas thrust for exhaust process completion. Consequently, the peak cylinder flow field pressure increased reflecting valve thickness. Comparison indicates that the relative pressure drop peaks before valve lift; for instance, the difference between the two timings was 0.0004s for a 0.2mm valve and ~0.0008s for a 0.3mm. In summary, a 0.3mm thick valve displayed greater gas-blocking capacity.

C. Simulation results under different valve width

Three different width sections of reed valves were selected: 3.7mm, 3.6mm, and 3.5mm. This enables a comparative analysis of the differences between these thicknesses, ultimately leading to the selection of the optimal valve disc thickness. The simulation results for the valve disc were then assessed, taking into consideration the relative pressure loss and valve lift, as illustrated in Figure 5 below.

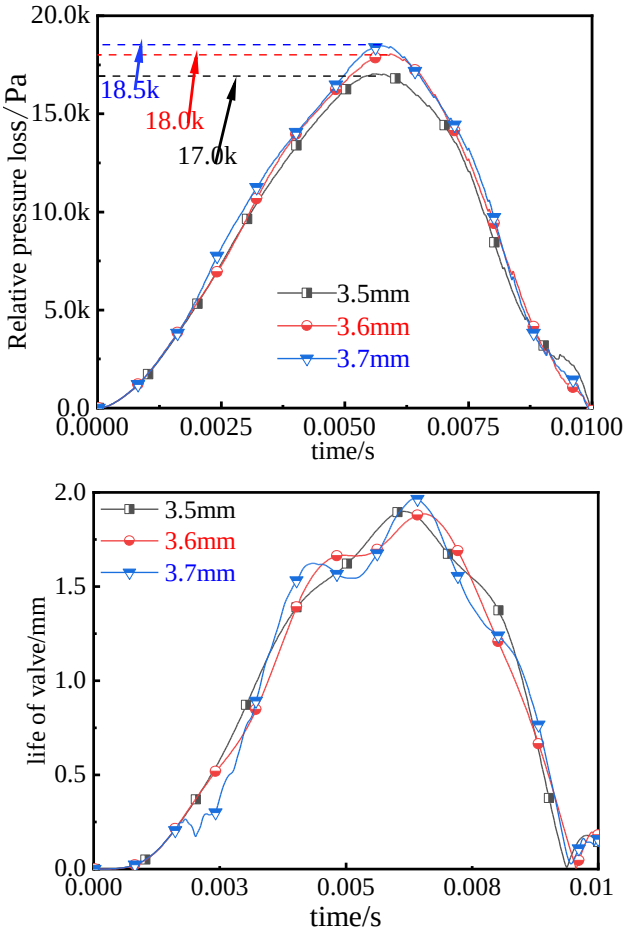

Fig. 5. Valve lift and pressure loss under two thicknesses

Simulated insights reveal the pressure drop across the

respective sections of three valve plates registering 18500Pa, 18000Pa & 17000Pa. Disc maxima are similar - 1.90mm, 1.88mm, & 1.97mm. As per the principle of deformation, increasing exhaust plate section width amplifies spring stiffness, thereby amplifying pressure loss. These trends mirror recurring patterns due to steady valve disc section widths. Peak valve lift curves signal wider sections leading to heightened vibrations, with opposing values noted at 3.7mm. This vibration translates into frequent expansions, reducing valve longevity and heightening pressure loss. Upon analysis, a 3.5mm valve slice section width is deemed suitable, effectively promoting longevity and reducing pressure wastage.

D. Simulation results under different valve thicknesses

Electromagnetic direct-drive air compressors must function within a specified range of exhaust pressures. Variations in exhaust pressure cause differences in pressure loss and valve lift during the exhaust process. To accurately simulate diverse exhaust pressures, this study utilized the gas compression model to calculate the cylinder volume for a specific exhaust pressure. By adjusting the initial calculation conditions and the fluid region's geometric model, we successfully simulated varied exhaust pressures. Specifically, we examined load and no-load conditions for exhaust pressures of 0.1 MPa and 0.5 MPa, respectively. See Table 2 for the initial conditions.

TABLE II
INITIAL CONDITIONS UNDER LOAD AND NO LOAD

	Initial pressure(MPa)	Total time(s)	Initial piston position(mm)
no-load	0.0	0.01	16
load	0.4	0.0036	4.6

Setting up the model with the initial conditions mentioned earlier is crucial for accurately simulating the behavior of the system under varying operational scenarios. By simulating the model under both loaded and unloaded conditions, we can gain valuable insights into how the system performs under different levels of demand.This simulation approach allows us to observe the valve lift and the relative pressure loss, which are key performance indicators for the air compressor. The curves obtained from these simulations, as depicted in Figure 6.

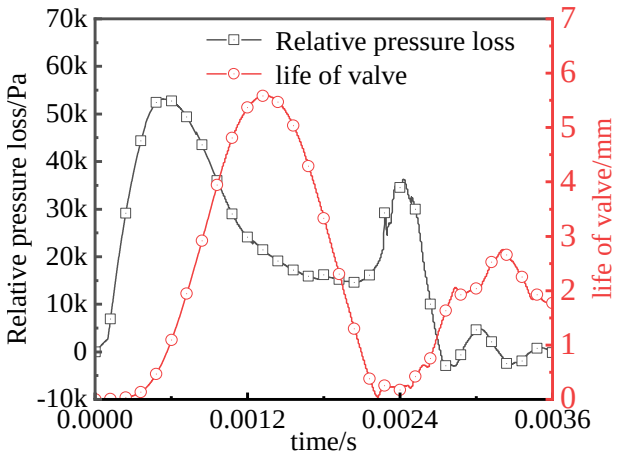

a) Exhaust pressure 0.5MPa

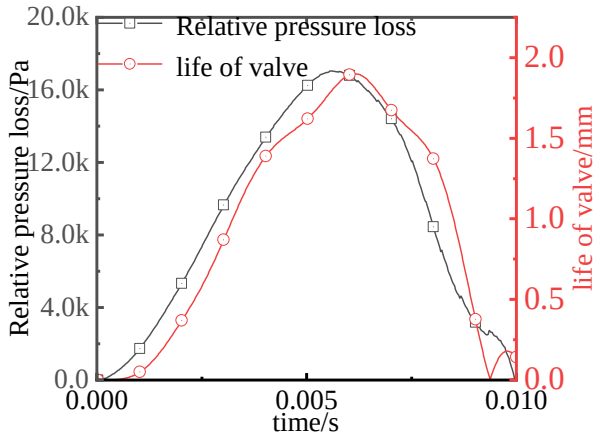

b) Exhaust pressure 0.1MPa

Fig.6. Valve lift and pressure loss under two thicknesses

The maximum pressure loss and maximum valve disc lift in the exhaust process are shown in Table 3:

TABLE III
MAXIMUM LIFT AND MAXIMUM RELATIVE PRESSURE LOSS OF VALVE DISC

Exhaust pressure(MPa)	Valve lift(mm)	Relative pressure loss(MPa)
0.1	1.8	0.017
0.5	5.6	0.054

The simulation results demonstrate that the valve disc exerts a more robust obstructive effect on the gas during loading, resulting in greater pressure loss. Specifically, the maximum pressure loss is 54KPa, while the pressure loss under no load is 17KPa. These values represent 10.8% and 17% of the exhaust pressure, respectively.

Under no load conditions, the relative pressure loss varies proportionally with the displacement of valve disc. Conversely, during loading, the valve plate's displacement curve lags behind the relative pressure loss curve. With no load present, the relative pressure loss curve and valve lift curve change gradually and essentially align with the mass flow curve of the air inlet. However, during loading, both the relative pressure loss and valve lift exhibit irregular fluctuations throughout the exhaust process, with the former experiencing more intense fluctuations in particular.

Further analysis indicates that in no-load conditions, the gas inlet's mass flow rate is minimal and changes gradually, giving the valve disc ample time to deform. This is demonstrated by the fact that the valve disc's displacement essentially changes synchronously with the relative pressure drop. Under load conditions, during the initial exhaust process, the gas inlet's mass flow rate is high, and the valve plate lacks sufficient time to deform, leading to notable obstruction of the gas flow and a significant relative pressure loss. As the valve lift increases and the mass flow rate at the inlet decreases, the relative pressure loss decreases quickly. Due to its elasticity, during the latter half of the exhaust process, as the gas inlet's mass flow rate decreases, the valve lift and relative pressure loss increase, resulting in the valve disc opening twice. The valve disc's lift during the second opening is lesser than during the first and does not close in time during the final exhaust process. When there is no load, the valve disc has little impact on obstructing gas flow and can open and close promptly. However, under a load, due to the limited exhaust process time, the valve disc's deformation

is not immediate, resulting in substantial pressure loss when the valve disc opens twice. Additionally, the valve disc cannot close promptly, leading to a minor backflow phenomenon. The valve disc blocks gas to some degree, mainly when there is significant exhaust pressure.

IV. Carrying Experimental Platforms

E. Experimental setup

This article utilizes a real-time digital control system named RTU-BOX. The hardware controller, assembled using multi-core heterogenous technology, includes a DSP, an ARM, and various FPGA cores. The primary processor utilized, the high-performing TMS320C28346 from Delfino platform, operates at 300MHz. Shown below is the instrument used for experimentation.

The testing apparatus employs a reliable real-time digital control system known for top-notch performance. The controller is fabricated with multi-core heterogeneous technology ensuring superior data processing efficiency. The core features multiple processors, such as DSP, ARM, and FPGA, with the primary one being the prestigious TMS320C28346 from Delfino platform. Operating at 300MHz, it ensures optimal speed in data processing. The experiment utilized the depicted equipment, successfully meeting study aims.

During use, the platform exhibited exceptional data processing capabilities, displaying low latency. Prior to commencement, all hardware parts underwent rigorous confirmation and tests for consistent, uninterrupted operation throughout the experiment. During the process, operators tracked progress via a live monitoring system to ascertain parameter compliance. Further safeguarding data precision, experiments were duplicated numerous times for statistical scrutiny under controlled conditions. Accuracy was ensured via the exact recalibration of the pressure sensor on sensing pressures at both the inlet and outlet of the compressor. Throughout the process, researchers attentively monitored sensor readings to swiftly detect and rectify anomalies, resulting in high-quality data acquisition.

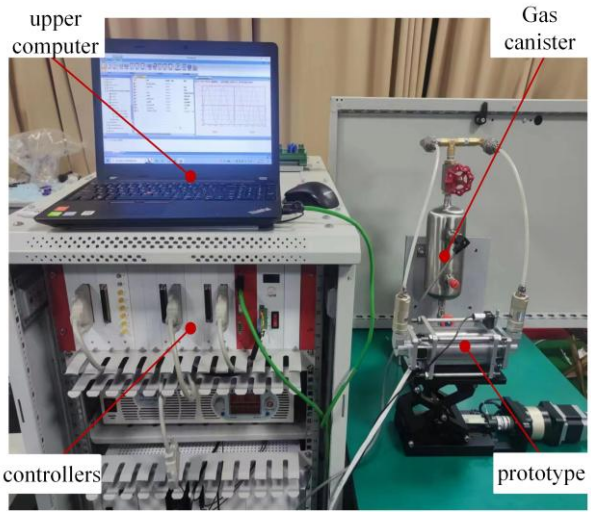

Fig. 7. Experimental platform

During the process of data acquisition, handling, and experimentation, precise pressure readings were obtained through use of sensors strategically positioned at both the intake and exhaust points. A series of identical trials were performed to consolidate the data generated.

Data Examination:

The captured footage was scrutinized through the application of motion tracking software to ascertain the precise valve displacement per unit time.

The recorded pressure levels were cross-referenced with the valve displacement data to guarantee precision correlations. Reliable outcomes were achieved by averaging pertinent information garnered from a minimum of five separate experimental iterations, thereby attenuating random anomalies. A multitude of experiments were executed under constant conditions to ascertain result reproducibility and accuracy. Disparity between various trial results was checked for consistency as illustrated in Diagram 7. Statistical data compiled from multipled runs is summarized in Table 4, showcasing the uniformity observed.

F. Analysis of experimental results

Upon successful execution of the previously mentioned configurations, the application must be initiated to ascertain a simulation outcome pertaining to the valve disc. The experimental outcomes reveal that the relative pressure loss profile and lift curve of the valve plate exhibit seamless transition when devoid of any load, thereby exhibiting negligible impediment on the gaseous flow whilst efficiently regulating its flow initiation and termination. Although the empirical observations demonstrate that the relative pressure loss and valve lift exceed those attained through simulations, the latter does incorporate some margin of error.

Potential explanations for this margin of error could encompass:

(1) Discrepancies stemming from machining procedures or frictional elements present between the constituents of the linear compressor,

(2) Datum divergence potentially attributed to vibrations emanating from the linear compressor leading to displacement of the laser sensor during experimentation,

(3) Deviation induced by the separation occurring between the pistons and the cylinder.

Towards rectifying these anomalies:

(1) Sensors were calibrated prior to commencing each experiment.

(2) Precision components were adopted to minimize machining variances.

(3) Data were collected numerous times and averaged to mitigate random variations.

Figure 7 displays the results from a single experimental trial, providing a clear picture of the system's behavior under test conditions. The data gathered from this trial confirm that in no-load situations, the valve disc is capable of making swift adjustments without causing a substantial impact on the gas flow. This rapid response is a critical characteristic for ensuring efficient operation and minimal energy loss.

Furthermore, Table 4 compiles a comprehensive summary of the experimental data collected across multiple trials. This aggregation of results offers a robust basis for analysis, highlighting the consistency in valve lift and pressure loss measurements across different tests. The consistency observed in these metrics is indicative of the system's reliability and the accuracy of the experimental setup. The detailed encapsulation of these findings in Table 4

serves as a valuable reference for further studies and design optimizations.

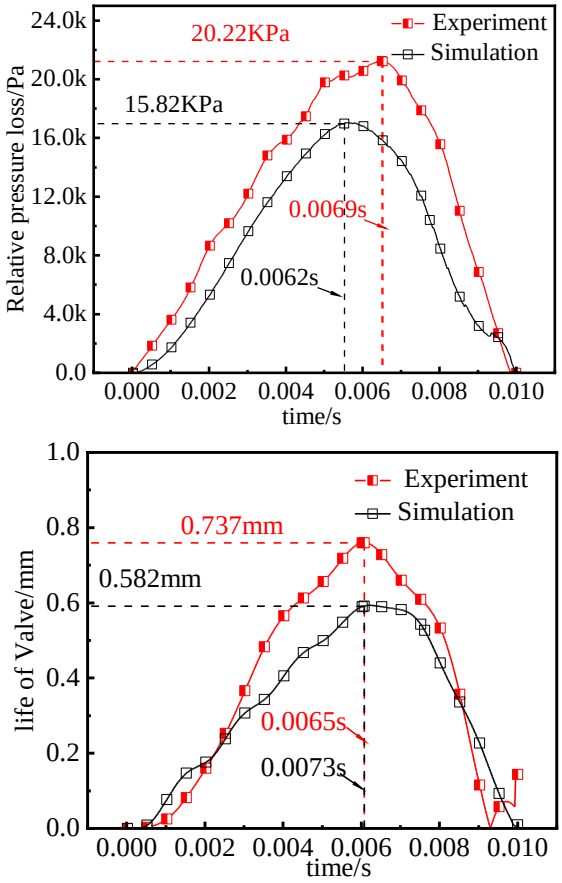

Fig. 7. Experimental result

TABLE IV
MAXIMUM LIFT AND MAXIMUM RELATIVE PRESSURE LOSS OF VALVE DISC

Valve life(mm)	Relative pressure loss(MPa)
1.8	0.017
1.79	0.0168
1.83	0.0171
1.8	0.017
1.79	1.0169

FIG.8 shows the valve lift and relative pressure loss curves under different load conditions tested. Performance analysis under different load conditions can reveal potential failure modes.

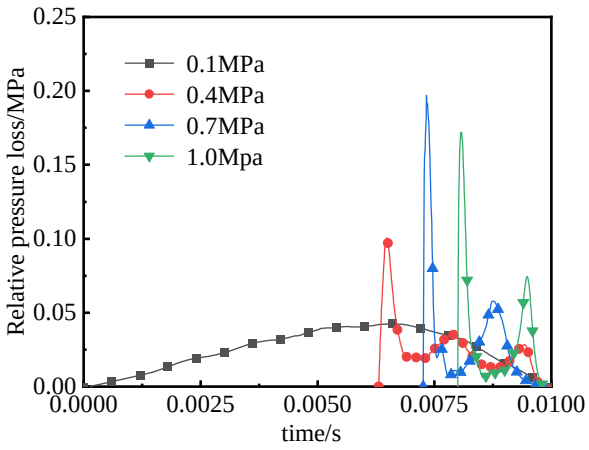

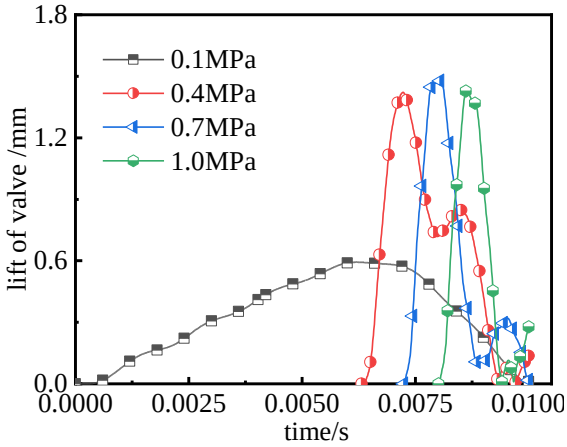

Fig. 8. the valve lift and relative pressure loss curves under different load conditions

The maximum pressure loss and maximum valve disc lift during the exhaust process are shown in Table 5:

TABLE V
MAXIMUM LIFT AND MAXIMUM RELATIVE PRESSURE LOSS OF VALVE DISC

Exhaust pressure(MPa)	Valve lift(mm)	Relative pressure loss(MPa)
0.1	0.59	0.04
0.4	1.42	0.10
0.7	1.48	0.19
1.0	1.43	0.17

When the exhaust pressure is 0.7 MPa, both the relative pressure loss and valve plate displacement reach their maximum values. The maximum valve lift and relative pressure loss initially increase and then decrease with the rise in exhaust pressure. Notably, the curves for an exhaust pressure of 0.1 MPa differ significantly from those under other conditions. At an exhaust pressure of 0.1 MPa, the relative pressure loss curve and the valve lift curve exhibit stable changes, primarily following the variation of the gas mass flow rate curve at the intake port. Under other conditions, both the relative pressure loss and valve lift experience fluctuations during the exhaust process, with the relative pressure loss showing more pronounced oscillations.

V. Conclusion

This study investigated the behavior of valve disc displacement and relative pressure loss under different parameters using an established fluid-structure coupling model. The following conclusions were drawn:

The transient numerical simulation of the flow field in the exhaust process of the electromagnetic direct-drive air compressor was carried out using the fluid-structure coupling method. The simulation results revealed that a vortex is generated above the valve disc during the process, and the gas impact is a significant factor responsible for keeping the valve disc open.

The study analyzed the relative pressure loss and valve lift curves in relation to valve disc thickness and section width. The results showed that a valve thickness of 0.2mm and a section width of 3.5mm result in less airflow obstruction. Under no-load conditions, the valve disc had minimal obstruction to gas flow and could open and close in time. However, under load conditions, the valve disc did not deform in time, resulting in large pressure loss at the beginning. In some instances, the valve disc opened twice, and closure was delayed, resulting in a slight reflux

phenomenon.

In conclusion, the established fluid-structure coupling model helped to analyze valve disc behavior under various parameters, providing valuable insights into the functioning of the electromagnetic direct drive air compressor. The findings of this study can inform future research on improving the overall efficiency and performance of these devices.

REFERENCES

[1] Y. Wang et al., "Experimental investigation on valve impact velocity and inclining motion of a reciprocating compressor," Applied Thermal Engineering, vol. 61, no. 2, pp. 149-156, 2013.

[2] B. Min et al., "Geometric correlation of discharge coefficients for discharge valve system in rolling piston rotary compressor," Journal of Mechanical Science and Technology, vol. 32, no. 8, pp. 3943-3954, 2018.

[3] Y. P. Deng et al., "Numerical Analysis on Efficiency of a Miniature High Pressure Compressor," Chinese Hydraulics & Pneumatics, no. 11, pp. 63-68, 2019.

[4] J. S. Kopppula, T. K. R. Rajagopal, and E. Gundabattini, "Correlating the experiment and fluid structure interaction results of a suction valve model from a hermetic reciprocating compressor," SAE Technical Paper, no. 2017-28-1948, 2017.

[5] F. Wang and L. L. Li, "Research on parameter matching and optimization of pure electric vehicle power system," Agricultural Equipment and Vehicle Engineering, vol. 58, no. 12, pp. 93-97, 2020.

[6] W. J. Deng et al., "CFD-based Performance Analysis of a Discharge Valve Plate in the Rolling Rotor Compressor," Journal of Northeastern University (Natural Science), vol. 41, no. 12, pp. 1754-1759, 2020.

[7] B. K. Han et al., "Research on flow field characteristics of suction valve of reciprocating compressor based on fluid-structure coupling method," Fluid Machinery, vol. 49, no. 5, pp. 47-53, 2021.

[8] H. Bao et al., "Analysis and Research on Flow Field Characteristics in Cylinder of Reciprocating Refrigeration Compressor," Fluid Machinery, vol. 48, no. 7, pp. 22-26, 2020.

[9] J. Ding et al., "Numerical analysis of motion characteristics of suction reed valve in DC linear compressor," Fluid Machinery, vol. 49, no. 7, pp. 38-44, 2021.

[10] X. Y. Zhang et al., "Theoretical analysis of dynamic characteristics in linear compressors," International Journal of Refrigeration, vol. 109, pp. 114-127, 2020.

[11] A. Bijanzad et al., "Development of a new moving magnet linear compressor. Part A: Design and modeling," International Journal of Refrigeration, vol. 113, pp. 70-79, 2020.

[12] Y. W. Liu et al., "Modification of shear stress transport turbulence model using helicity for predicting corner separation flow in a linear compressor cascade," Journal of Turbomachinery, vol. 142, no. 2, 2020.

[13] Y. L. Liu et al., "Experimental investigation of the discharge valve dynamics in an oil-free linear compressor for Joule-Thomson throttling refrigerator," Applied Thermal Engineering, vol. 209, 2022.

[14] Q. Huang et al., "Experimental investigation on piston offset and performance of helium valved linear compressor with an external gas bypass," International Journal of Refrigeration, vol. 145, pp. 417-424, 2023.

[15] C. Z. Li et al., "Characteristic analysis and energy efficiency of an oil-free dual-piston linear compressor for household refrigeration with various conditions," Energy, vol. 270, 2023.

[16] M. Faisal, M. Afzal, and T. Khan, "Introduction to Linear Compressor and Electronics Cooling—A Review," Emerging Trends in Mechanical and Industrial Engineering: Select Proceedings of ICETMIE 2022, pp. 331-343, 2023.

[17] Z. J. Huang et al., "Theoretical and Experimental Investigation on Comparing the Efficiency of a Single-Piston Valved Linear Compressor and a Symmetrical Dual-Piston Valved Linear Compressor," Energies, vol. 15, no. 22, 2022.

[18] I. S. Hwang and Y. L. Lee, "Study on the performance of linear compressor with suction system shapes using a transient CFD model," Journal of Mechanical Science and Technology, vol. 36, no. 4, pp. 1809-1816, 2022.

[19] A. Ahmad et al., "Performance Analysis of Tubular Moving Magnet Linear Oscillating Actuator for Linear Compressors," Energies, vol. 15, no. 9, 2022.

[20] S. P. Hu et al., "Moving magnet linear oscillation motor electromagnetic system theory and experiment," Mechanical Design and Research, vol. 39, no. 2, pp. 202-206, 2023.

[21] H. Lin et al., "Analytical Solution for Electromagnetic Performance Analysis of Permanent Magnet Synchronous Motor with a Parallel Magnetized Cylindrical Permanent Magnet," Machines, vol. 12, no. 1, pp. 34-45, 2024.

[22] A. M. Maghfiroh and A. B. Chandra, "Thermo Valve Air Compressor Maintenance and Repair Using the Overall Equipment Effectiveness (OEE) Method in Maintenance," International Journal of Engineering Continuity, vol. 10, no. 1, pp. 45-56, 2023.

[23] Hoang, Long, Tien Long Banh, and Tuan-Linh Nguyen, "A new method for designing and machining air compressor screw pairs," International Journal of Modern Physics B, vol. 34, no. 22n24, pp. 2040128, 2020.